

Score-Based Turbo Message Passing for Plug-and-Play Compressive Imaging

Chang Cai, *Graduate Student Member, IEEE*, Hao Jiang, *Graduate Student Member, IEEE*,
Xiaojun Yuan, *Fellow, IEEE*, and Ying-Jun Angela Zhang, *Fellow, IEEE*

Abstract—Message-passing algorithms have been adapted for compressive imaging by incorporating various off-the-shelf image denoisers. However, these denoisers rely largely on generic or hand-crafted priors and often fall short in accurately capturing the complex statistical structure of natural images. As a result, traditional plug-and-play (PnP) methods often lead to suboptimal reconstruction, especially in highly underdetermined regimes. Recently, score-based generative models have emerged as a powerful framework for accurately characterizing sophisticated image distribution. Yet, their direct use for posterior sampling typically incurs prohibitive computational complexity. In this paper, by exploiting the close connection between score-based generative modeling and empirical Bayes denoising, we devise a message-passing framework that integrates a score-based minimum mean-squared error (MMSE) denoiser for compressive image recovery. The resulting algorithm, named score-based turbo message passing (STMP), combines the fast convergence of message passing with the expressive power of score-based generative priors. For practical systems with quantized measurements, we further propose quantized STMP (Q-STMP), which augments STMP with a component-wise MMSE dequantization module. We demonstrate that the asymptotic performance of STMP and Q-STMP can be accurately predicted by a set of state-evolution (SE) equations. Experiments on the FFHQ dataset demonstrate that STMP strikes a significantly better performance-complexity tradeoff compared with competing baselines, and that Q-STMP remains robust even under 1-bit quantization. Remarkably, both STMP and Q-STMP typically converge within 10 iterations.

Index Terms—Message passing, score-based generative priors, diffusion models, compressive image recovery, quantization.

I. INTRODUCTION

Compressive image recovery [2] refers to the reconstruction of high-dimensional images from a reduced set of (possibly linear) measurements. This paradigm underlies a broad range of practical systems including magnetic resonance imaging (MRI) [3], synthetic aperture radar (SAR) [4], and computed tomography (CT) [5], where physical constraints or hardware limitations restrict the number of available measurements. As

An earlier version of this paper was presented in part at IEEE 26th International Workshop on Signal Processing and Artificial Intelligence for Wireless Communications (SPAWC), 2025 [1].

Chang Cai was with the Department of Information Engineering, The Chinese University of Hong Kong, Hong Kong, and is now with the Department of Electrical and Electronic Engineering, The University of Hong Kong, Hong Kong (e-mail: changcai@hku.hk).

Hao Jiang and Xiaojun Yuan are with the National Key Laboratory of Wireless Communications, University of Electronic Science and Technology of China, Chengdu 611731, China (e-mail: jh@std.uestc.edu.cn; xjyuan@uestc.edu.cn).

Ying-Jun Angela Zhang is with the Department of Information Engineering, The Chinese University of Hong Kong, Hong Kong (e-mail: yjzhang@ie.cuhk.edu.hk).

a result, the associated inverse problem is highly underdetermined. Successful image recovery thus requires incorporating strong prior knowledge of the underlying image to regularize the solution space.

Message passing provides a highly efficient paradigm for Bayesian compressive sensing (CS), enabling the principled incorporation of various sparsity-inducing priors. For linear inverse problems, representative algorithms include approximate message passing (AMP), turbo message passing (TMP) [6] (a.k.a. Turbo-CS), vector AMP (VAMP) [7], and orthogonal AMP (OAMP) [8]. These algorithms have also been extended beyond the linear setting, most notably through generalized AMP (GAMP) [9], which generalizes the framework to a broad class of generalized linear models (GLMs). However, since natural images do not have an exact sparse representation in any known transform domain, these sparsity-based approaches often exhibit poor performance in many imaging applications. To address this limitation, off-the-shelf image denoisers have been plugged into message-passing algorithms to enhance reconstruction performance, giving rise to methods such as denoising-based AMP (D-AMP) [2], denoising-based Turbo-CS (D-Turbo-CS) [10], and BM3D phase-retrieval GAMP (BM3D-prGAMP) [11]. Commonly used denoisers include total variation (TV), SURE-LET [12], and BM3D [13]. These off-the-shelf denoisers are non-parametric or heuristic in nature and do not rely on an explicit statistical model of the underlying image. While effective in practice, such plug-and-play (PnP) methods still fall short in fully exploiting the rich and highly structured priors inherent in natural images. To benefit from deep learning for more accurate prior modeling, methods such as learned D-AMP (LDAMP) [14] and AMP-Net [15] unroll message-passing iterations into layer-wise trainable architectures, in which traditional denoisers are replaced by convolutional neural network (CNN)-based modules. However, these approaches typically require training separate end-to-end models for different sampling ratios and noise levels, thereby limiting their flexibility and generalizability.

Recently, score-based generative models [16], [17] (a.k.a. diffusion models [18]) have achieved unparalleled success in generating high-quality samples across a wide range of domains, including images, videos, and molecular conformations. These results highlight their exceptional capacity to capture the complex structure of high-dimensional data distributions. During training, score-based generative models corrupt the data with random Gaussian noise of different magnitudes, and learn to approximate the gradient of the log-density of the perturbed data, known as the score function.

The score function is then applied at each reverse-diffusion step for sample generation. Score-based generative models can also be leveraged for solving inverse problems without task-specific training [19], [20], [21], [22], [23], [24], [25], [26]. These approaches combine a prior term provided by the learned score function with a likelihood term derived from the degradation model, forming a Bayesian posterior via Bayes' rule. Sampling from this posterior enables high-quality reconstructions across a variety of imaging tasks. However, these methods typically require traversing the full reverse-diffusion trajectory, often involving hundreds or even thousands of neural function evaluations (NFEs), which results in substantial computational cost.

To address the above limitations, we propose integrating score-based generative priors into the message-passing framework for compressive imaging. This hybrid approach inherits the fast convergence and computational efficiency of message passing while fully leveraging the expressive power of learned score networks to capture complex image priors. Specifically, we exploit the fact that, at each iteration, message-passing algorithms construct an additive white Gaussian noise (AWGN) observation of the ground-truth image. This enables the direct use of the score network for denoising via Tweedie's formula [27], with only one forward pass needed per iteration. In addition, we employ a second-order score network [28], [29] that outputs the diagonals of the log-density Hessian, allowing the calculation of the denoised variance required for message passing. These components together facilitate a turbo-type message-passing algorithm with score-based denoising, named score-based turbo message passing (STMP). Owing to its PnP structure, STMP naturally adapts to different sampling ratios and measurement noise levels without requiring retraining. In practice, measurements are often quantized due to the finite precision of analog-to-digital converters (ADCs) and data storage constraints. Motivated by expectation propagation (EP) [30] and its application to GLMs [31], we extend STMP to handle quantized measurements, resulting in the quantized STMP (Q-STMP) algorithm. Q-STMP iteratively exchanges messages between STMP and an additional dequantization module, each producing extrinsic estimates that serve as inputs to the other. Moreover, we characterize the asymptotic mean-squared error (MSE) performance of STMP and Q-STMP via state evolution (SE). The main contributions and results of this paper are summarized as follows.

- We propose STMP, a turbo-type message-passing algorithm that integrates score-based generative priors into TMP for compressive imaging. STMP achieves not only fast convergence but also high-fidelity reconstruction. Its asymptotic MSE performance is accurately characterized by SE.
- We develop Q-STMP for quantized compressive image recovery, which couples STMP with a minimum mean-squared error (MMSE) dequantization module. We derive the corresponding SE recursions that precisely track its asymptotic behavior in the large-system limit.
- Extensive experiments on the FFHQ dataset [32] demonstrate that STMP achieves state-of-the-art performance-

complexity tradeoffs compared with denoising-based message passing, regularized linear regression, and score-based posterior sampling schemes. Q-STMP remains robust even under 1-bit quantization. Notably, both algorithms typically converge in fewer than 10 iterations.

The rest of this paper is organized as follows. Section II reviews the related work. Section III introduces the basics of the TMP framework. In Section IV, we establish the connection between score functions and MMSE denoising, and describe the learning of the first- and second-order score models. Section V presents the proposed STMP algorithm and its SE characterization. In Section VI, we extend STMP to quantized systems, developing the Q-STMP algorithm and deriving its corresponding SE equations. Experimental results on compressive and quantized compressive imaging are provided in Section VII. Finally, Section VIII concludes the paper.

II. RELATED WORK

A. Optimization-Based PnP Methods

A large body of prior work approaches the maximum *a posteriori* (MAP) solution from an optimization perspective by formulating the linear inverse problem as a regularized least-squares program and solving it via proximal methods. Building on the denoising interpretation of alternating direction method of multipliers (ADMM), the PnP framework replaces explicit proximal operators with powerful image denoisers, leading to PnP-ADMM [33] and numerous related variants. Subsequent researches have analyzed convergence properties [34], proposed parameter-free solutions [35], and extended PnP-ADMM to online and large-scale imaging settings [36]. In addition, PnP versions of the half-quadratic splitting (HQS) algorithm and other variable-splitting schemes have been developed, exemplified by the PnP-HQS framework [37] and its extensions using deep denoisers [38]. In parallel, the regularization by denoising (RED) framework [39] explicitly constructs a regularizer whose gradient is linked to a chosen denoiser, allowing efficient implementation via first-order optimization methods. These formulations give rise to algorithms such as RED by fixed-point projection (RED-PRO) [40] and RED-ADMM [41].

B. Diffusion-Based PnP Methods

In diffusion-based inverse solvers, sampling from the exact posterior distribution is intractable due to the time dependence of the likelihood. This challenge has motivated a variety of approximation strategies. Score-based annealed Langevin dynamics (Score-ALD) [19] enforces data consistency via a matched-filter-like approximation of the likelihood score at each step. Iterative latent variable refinement (ILVR) [20] and pseudoinverse-guided diffusion models (IIGDM) [25] incorporate the Moore-Penrose pseudoinverse of the measurement operator to guide the reverse-diffusion trajectory toward the observation-consistent subspace. Diffusion model based posterior sampling (DMPS) [21] employs a linear MMSE (LMMSE)-type approximation of the likelihood score. Reverse mean propagation (RMP) [42] optimizes the reverse Kullback-Leibler (KL) divergence with nature gradient descent and

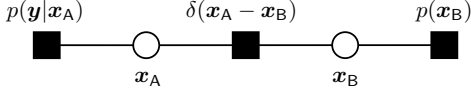


Fig. 1. Factor graph for TMP derivation. The circles represent variable nodes and the squares represent factor nodes.

propagates the mean at each reverse step. These approaches typically introduce additional hyperparameters that are sensitive and require careful tuning. The approximation errors accumulate over iterations and can potentially drive the trajectory away from the underlying data manifold. To mitigate this issue, manifold constrained gradient (MCG) [23] introduces an additional correction term that can be seamlessly integrated with existing solvers to steer the iterates back toward the data manifold. Diffusion posterior sampling (DPS) [24] generalizes the above work to nonlinear inverse problems, which requires backpropagation through the unconditional score network to compute likelihood gradients. Most of the above methods require hundreds to thousands of reverse-diffusion steps, resulting in significant computational burden. Denoising diffusion restoration models (DDRM) [22] alleviates this cost by employing denoising diffusion implicit models (DDIM) [43], an ordinary differential equation (ODE)-based accelerated sampler, enabling high-quality reconstructions with as few as 20 NFEs. DiffPIR [26] operates in an optimization-inspired PnP-HQS framework. At each iteration, it heuristically injects Gaussian noise following diffusion principles to improve flexibility, which in turn often slows convergence. Meanwhile, variational-inference approaches such as RED-diff [44] reinterpret diffusion priors through the lens of the RED framework, offering a complementary optimization-based perspective.

C. Quantized Compressive Sensing

Early efforts in quantized compressed sensing focused on adapting classical sparse recovery algorithms to low-bit measurements, leading to methods such as quantized subspace pursuit (QSP), quantized iterative hard thresholding (QIHT), and quantized compressive sampling matching pursuit (QCoSaMP), as surveyed in [45]. A seminal contribution from the message-passing perspective is message-passing dequantization (MPDQ) [46], which incorporates regular and non-regular scalar quantizers into the GAMP framework. Building on the turbo principle, generalized turbo signal recovery (GTurbo-SR) [47] adapts Turbo-CS to quantized measurements by introducing an additional component-wise MMSE denoiser tailored to the quantization likelihood. A further unifying perspective is offered by the Bayesian inference framework in [31], which generalizes EP to arbitrary GLMs. Recently, the advent of score-based generative models has inspired new approaches to quantized compressed sensing. QCS-SGM [48] formulates quantized recovery as posterior sampling using a learned score prior, while QCS-SGM+ [49] extends this framework beyond row-orthogonal sensing matrices for broader applicability.

III. TMP FRAMEWORK

In this section, we briefly review the TMP framework [6] for solving linear inverse problems based on an EP-type message-

Algorithm 1: TMP Framework

```

1: Input:  $\mathbf{A}$ ,  $\mathbf{y}$ ,  $\delta_0^2$ ,  $\mathbf{x}_A^{\text{pri}}$ ,  $v_A^{\text{pri}}$ 
2: Output:  $\mathbf{x}_B^{\text{post}}$ 
3: repeat
4:   % LMMSE estimator (module A)
5:    $\mathbf{x}_A^{\text{post}} = \mathbf{x}_A^{\text{pri}} + \frac{v_A^{\text{pri}}}{v_A^{\text{pri}} + \delta_0^2} \mathbf{A}^\top (\mathbf{y} - \mathbf{A}\mathbf{x}_A^{\text{pri}})$ 
6:    $v_A^{\text{post}} = v_A^{\text{pri}} - \frac{M}{N} \frac{(v_A^{\text{pri}})^2}{v_A^{\text{pri}} + \delta_0^2}$ 
7:    $v_B^{\text{pri}} = v_A^{\text{ext}} = \left( \frac{1}{v_A^{\text{post}}} - \frac{1}{v_A^{\text{pri}}} \right)^{-1}$ 
8:    $\mathbf{x}_B^{\text{pri}} = \mathbf{x}_A^{\text{ext}} = v_A^{\text{ext}} \left( \frac{\mathbf{x}_A^{\text{post}}}{v_A^{\text{post}}} - \frac{\mathbf{x}_A^{\text{pri}}}{v_A^{\text{pri}}} \right)$ 
9:   % MMSE denoiser (module B)
10:   $\mathbf{x}_B^{\text{post}} = \mathbb{E}[\mathbf{x}_B | \mathbf{x}_B^{\text{pri}}]$ 
11:   $v_B^{\text{post}} = \frac{1}{N} \text{tr}(\text{Cov}[\mathbf{x}_B | \mathbf{x}_B^{\text{pri}}])$ 
12:   $v_A^{\text{pri}} = v_B^{\text{ext}} = \left( \frac{1}{v_B^{\text{post}}} - \frac{1}{v_B^{\text{pri}}} \right)^{-1}$ 
13:   $\mathbf{x}_A^{\text{pri}} = \mathbf{x}_B^{\text{ext}} = v_B^{\text{ext}} \left( \frac{\mathbf{x}_B^{\text{post}}}{v_B^{\text{post}}} - \frac{\mathbf{x}_B^{\text{pri}}}{v_B^{\text{pri}}} \right)$ 
14: until the stopping criterion is met

```

passing derivation. Consider the real-valued linear model

$$\mathbf{y} = \mathbf{A}\mathbf{x} + \mathbf{n}, \quad (1)$$

where $\mathbf{x} \in \mathbb{R}^N$ is an unknown signal vector, $\mathbf{y} \in \mathbb{R}^M$ denotes noisy linear measurements, \mathbf{A} is a known measurement matrix, and $\mathbf{n} \sim \mathcal{N}(\mathbf{0}, \delta_0^2 \mathbf{I})$ is an AWGN. The goal is to recover \mathbf{x} from \mathbf{y} , particularly in the underdetermined regime where $M < N$.

TMP solves the above problem by evaluating the posterior distribution, which can be factorized as

$$p(\mathbf{x} | \mathbf{y}) \propto p(\mathbf{x})p(\mathbf{y} | \mathbf{x}). \quad (2)$$

By letting $\mathbf{x}_A = \mathbf{x}_B = \mathbf{x}$, we obtain an equivalent factorization of (2):

$$p(\mathbf{x}_A, \mathbf{x}_B | \mathbf{y}) \propto p(\mathbf{x}_B) \delta(\mathbf{x}_A - \mathbf{x}_B) p(\mathbf{y} | \mathbf{x}_A), \quad (3)$$

where $\delta(\cdot)$ is the Dirac delta function. The corresponding factor graph is illustrated in Fig. 1.

We start by initializing the message from the factor node $\delta(\mathbf{x}_A - \mathbf{x}_B)$ to the variable node \mathbf{x}_A as $\mu_{\delta \rightarrow \mathbf{A}}(\mathbf{x}_A) = \mathcal{N}(\mathbf{x}_A; \mathbf{x}_A^{\text{pri}}, v_A^{\text{pri}} \mathbf{I})$. According to EP, the belief on \mathbf{x}_A is given by $b(\mathbf{x}_A) = \mathcal{N}(\mathbf{x}_A; \mathbf{x}_A^{\text{post}}, \mathbf{V}_A^{\text{post}}) = \text{proj}_G[p(\mathbf{y} | \mathbf{x}_A) \mu_{\delta \rightarrow \mathbf{A}}(\mathbf{x}_A)]$, where $\text{proj}_G[\cdot]$ represents the projection of a probability distribution to a Gaussian density with matched first- and second-order moments. By noting that the product of two Gaussian messages is proportional to a Gaussian probability density function (PDF), the projection in $b(\mathbf{x}_A)$ can thus be removed. TMP further approximates $\mathbf{V}_A^{\text{post}}$ using a shared scalar variance [6], resulting in the belief of the form $b(\mathbf{x}_A) \approx \mathcal{N}(\mathbf{x}_A; \mathbf{x}_A^{\text{post}}, v_A^{\text{post}} \mathbf{I})$, where

$$\mathbf{x}_A^{\text{post}} = \mathbf{x}_A^{\text{pri}} + v_A^{\text{pri}} \mathbf{A}^\top (v_A^{\text{pri}} \mathbf{A} \mathbf{A}^\top + \delta_0^2 \mathbf{I})^{-1} (\mathbf{y} - \mathbf{A} \mathbf{x}_A^{\text{pri}}), \quad (4)$$

$$v_A^{\text{post}} = v_A^{\text{pri}} - \frac{(v_A^{\text{pri}})^2}{N} \text{tr} \left(\mathbf{A}^\top (v_A^{\text{pri}} \mathbf{A} \mathbf{A}^\top + \delta_0^2 \mathbf{I})^{-1} \mathbf{A} \right). \quad (5)$$

Eqns. (4) and (5) are the posterior mean and variance from the LMMSE estimator of \mathbf{x}_A , respectively. In compressive imaging, the measurement matrix \mathbf{A} is typically partial orthogonal (i.e., $\mathbf{A}\mathbf{A}^\top = \mathbf{I}$), constructed by randomly selecting rows from an orthogonal transform such as the discrete cosine transform (DCT), discrete Fourier transform (DFT), or Hadamard matrix. The partial orthogonality of \mathbf{A} enables the simplifications shown in Lines 5 and 6 of Algorithm 1. The message passed from the variable node \mathbf{x}_A to the factor node $\delta(\mathbf{x}_A - \mathbf{x}_B)$, referred to as the extrinsic message, is given by $\mu_{A \rightarrow \delta}(\mathbf{x}_A) = \mathcal{N}(\mathbf{x}_A; \mathbf{x}_A^{\text{ext}}, v_A^{\text{ext}} \mathbf{I}) = \mathcal{N}(\mathbf{x}_A; \mathbf{x}_A^{\text{post}}, v_A^{\text{post}} \mathbf{I}) / \mathcal{N}(\mathbf{x}_A; \mathbf{x}_A^{\text{pri}}, v_A^{\text{pri}} \mathbf{I})$. This yields the update rules in Lines 7 and 8 of Algorithm 1.

The message $\mu_{A \rightarrow \delta}(\mathbf{x}_A) = \mathcal{N}(\mathbf{x}_A; \mathbf{x}_A^{\text{ext}}, v_A^{\text{ext}} \mathbf{I})$ flows rightward through the factor node $\delta(\mathbf{x}_A - \mathbf{x}_B)$ unchanged, manifesting as $\mu_{\delta \rightarrow B}(\mathbf{x}_B) = \mathcal{N}(\mathbf{x}_B; \mathbf{x}_B^{\text{pri}}, v_B^{\text{pri}} \mathbf{I})$ on the other side. The belief on \mathbf{x}_B is calculated as $b(\mathbf{x}_B) = \mathcal{N}(\mathbf{x}_B; \mathbf{x}_B^{\text{post}}, \mathbf{V}_B^{\text{post}}) = \text{proj}_G [p(\mathbf{x}_B) \mu_{\delta \rightarrow B}(\mathbf{x}_B)]$, where

$$\begin{aligned} \mathbf{x}_B^{\text{post}} &= \frac{1}{Z} \int \mathbf{x}_B p(\mathbf{x}_B) \mathcal{N}(\mathbf{x}_B; \mathbf{x}_B^{\text{pri}}, v_B^{\text{pri}} \mathbf{I}) d\mathbf{x}_B, \\ \mathbf{V}_B^{\text{post}} &= \frac{1}{Z} \int (\mathbf{x}_B - \mathbf{x}_B^{\text{pri}})(\mathbf{x}_B - \mathbf{x}_B^{\text{pri}})^\top \\ &\quad \times p(\mathbf{x}_B) \mathcal{N}(\mathbf{x}_B; \mathbf{x}_B^{\text{pri}}, v_B^{\text{pri}} \mathbf{I}) d\mathbf{x}_B, \end{aligned} \quad (6)$$

with $Z = \int p(\mathbf{x}_B) \mathcal{N}(\mathbf{x}_B; \mathbf{x}_B^{\text{pri}}, v_B^{\text{pri}} \mathbf{I}) d\mathbf{x}_B$ being the normalization constant. It is known that the error vector $\mathbf{x}_B^{\text{pri}} - \mathbf{x}_B$ is asymptotically independent and identically distributed (i.i.d.) Gaussian as $M, N \rightarrow \infty$ with a fixed ratio [50]. Therefore, TMP models $\mathbf{x}_B^{\text{pri}}$ as an AWGN observation of the ground-truth signal \mathbf{x}_B :

$$\mathbf{x}_B^{\text{pri}} = \mathbf{x}_B + \mathbf{w}, \quad \mathbf{w} \sim \mathcal{N}(\mathbf{0}, v_B^{\text{pri}} \mathbf{I}). \quad (8)$$

From (8), we have $p(\mathbf{x}_B^{\text{pri}} | \mathbf{x}_B) = \mathcal{N}(\mathbf{x}_B^{\text{pri}}; \mathbf{x}_B, v_B^{\text{pri}} \mathbf{I})$. By noting that $\mathcal{N}(\mathbf{x}_B; \mathbf{x}_B^{\text{pri}}, v_B^{\text{pri}} \mathbf{I})$ in (6) and (7) takes the same form as $p(\mathbf{x}_B^{\text{pri}} | \mathbf{x}_B)$, the belief update on \mathbf{x}_B can be interpreted as an MMSE denoising problem under the AWGN observation model (8), i.e.,

$$\mathbf{x}_B^{\text{post}} = \mathbb{E}[\mathbf{x}_B | \mathbf{x}_B^{\text{pri}}], \quad (9)$$

$$\mathbf{V}_B^{\text{post}} = \text{Cov}[\mathbf{x}_B | \mathbf{x}_B^{\text{pri}}]. \quad (10)$$

Similarly, we approximate $\mathbf{V}_B^{\text{post}}$ by $v_B^{\text{post}} \mathbf{I}$ with $v_B^{\text{post}} = \text{tr}(\text{Cov}[\mathbf{x}_B | \mathbf{x}_B^{\text{pri}}]) / N$ to simplify the computation. The extrinsic message of \mathbf{x}_B is denoted as $\mu_{B \rightarrow \delta}(\mathbf{x}_B) = \mathcal{N}(\mathbf{x}_B; \mathbf{x}_B^{\text{ext}}, v_B^{\text{ext}} \mathbf{I})$, where the variance and mean are respectively given in Lines 12 and 13 of Algorithm 1. Finally, the extrinsic message of \mathbf{x}_B flows leftward through the factor node $\delta(\mathbf{x}_A - \mathbf{x}_B)$ unchanged, serving as the prior message of \mathbf{x}_A in the next iteration, i.e., $\mathbf{x}_A^{\text{pri}} = \mathbf{x}_B^{\text{ext}}, v_A^{\text{pri}} = v_B^{\text{ext}}$.

As shown in Algorithm 1, the above TMP framework admits a modularized interpretation that resembles the turbo decoder [51], which consists of two modules. Module A is an LMMSE estimator of \mathbf{x} based on the observation \mathbf{y} , in which the messages from module B serve as the prior mean and variance. With the equivalent AWGN observation model (8), Module B is an MMSE denoiser incorporating the prior distribution of \mathbf{x} and the messages from module A. The two modules are executed iteratively to refine the estimate of \mathbf{x} .

The main challenge in implementing the TMP framework arises from the MMSE denoising part in module B, primarily due to i) the lack of a tractable prior image distribution, and ii) the high-dimensional integrals involved in calculating the posterior mean and variance. To sidestep these difficulties, various off-the-shelf image denoisers (e.g., TV, SURE-LET [12], BM3D [13]) are plugged into message-passing algorithms in place of the MMSE denoiser. These PnP denoisers typically rely on generic or hand-crafted priors, which could lead to substantial imperfection in compressive imaging applications due to the oversimplification or misspecification of the prior distribution. Motivated by the above, we propose the integration of score-based generative models into TMP as accurate and expressive image priors, leading to a data-driven Bayesian inference approach to compressive imaging.

IV. LEARNING SCORE-BASED GENERATIVE PRIORS FOR MMSE DENOISING

A. Bridging Score Function and MMSE Denoising

Theorem 1 (Tweedie's formula [27], [52] and its second-order generalization [28]). *Consider $\tilde{\mathbf{x}}$ to be an AWGN observation of \mathbf{x} , i.e., $\tilde{\mathbf{x}} = \mathbf{x} + \mathbf{w}$, where the prior distribution $p(\mathbf{x})$ and the noise distribution $\mathbf{w} \sim \mathcal{N}(\mathbf{0}, \sigma^2 \mathbf{I})$ are given. The posterior mean and covariance are respectively given by*

$$\mathbb{E}[\mathbf{x} | \tilde{\mathbf{x}}] = \tilde{\mathbf{x}} + \sigma^2 \nabla_{\tilde{\mathbf{x}}} \log p(\tilde{\mathbf{x}}), \quad (11)$$

$$\text{Cov}[\mathbf{x} | \tilde{\mathbf{x}}] = \sigma^2 \mathbf{I} + \sigma^4 \nabla_{\tilde{\mathbf{x}}}^2 \log p(\tilde{\mathbf{x}}). \quad (12)$$

Theorem 1 bridges score-based generative modeling and empirical Bayes method, providing the theoretical foundation for using score functions to perform MMSE denoising of AWGN observations. With the score functions available, Theorem 1 enables the efficient implementation of the MMSE denoiser in (9) and (10). We next discuss how to obtain the first- and second-order score estimates, $\nabla_{\tilde{\mathbf{x}}} \log p(\tilde{\mathbf{x}})$ and $\nabla_{\tilde{\mathbf{x}}}^2 \log p(\tilde{\mathbf{x}})$, via the denoising score matching technique [16], [53].

B. First-Order Score Matching

For a given σ , we aim to learn a first-order score model $\mathbf{s}_\theta(\cdot, \sigma^2) : \mathbb{R}^N \rightarrow \mathbb{R}^N$ parameterized by θ with the following score matching objective:

$$\min_{\theta} \mathbb{E}_{p(\tilde{\mathbf{x}})} \left[\left\| \mathbf{s}_\theta(\tilde{\mathbf{x}}, \sigma^2) - \nabla_{\tilde{\mathbf{x}}} \log p(\tilde{\mathbf{x}}) \right\|_2^2 \right]. \quad (13)$$

The above formulation is shown equivalent to the denoising score matching objective [16], [53], given by

$$\min_{\theta} \mathbb{E}_{p(\mathbf{x})p(\tilde{\mathbf{x}}|\mathbf{x})} \left[\left\| \mathbf{s}_\theta(\tilde{\mathbf{x}}, \sigma^2) - \nabla_{\tilde{\mathbf{x}}} \log p(\tilde{\mathbf{x}}|\mathbf{x}) \right\|_2^2 \right]. \quad (14)$$

Substituting $\nabla_{\tilde{\mathbf{x}}} \log p(\tilde{\mathbf{x}}|\mathbf{x}) = -\frac{\tilde{\mathbf{x}} - \mathbf{x}}{\sigma^2}$ into (14) yields

$$\min_{\theta} \ell_1(\theta; \sigma) \triangleq \mathbb{E}_{p(\mathbf{x})p(\tilde{\mathbf{x}}|\mathbf{x})} \left[\left\| \mathbf{s}_\theta(\tilde{\mathbf{x}}, \sigma^2) + \frac{\tilde{\mathbf{x}} - \mathbf{x}}{\sigma^2} \right\|_2^2 \right]. \quad (15)$$

In practice, the score-based MMSE denoiser is required to operate effectively across a range of noise levels. We therefore combine (15) for all possible $\sigma \in \{\sigma_i\}_{i=1}^L$ to formulate the

following unified objective for training the first-order score model:

$$\min_{\theta} \mathcal{L}_1(\theta; \{\sigma_i\}_{i=1}^L) \triangleq \frac{1}{L} \sum_{i=1}^L \lambda_1(\sigma_i) \ell_1(\theta; \sigma_i), \quad (16)$$

where $\lambda_1(\sigma_i)$ is the weighting factor depending on σ_i .

C. Second-Order Score Matching

For a given σ , we aim to learn a second-order score model $\mathcal{S}_\phi(\cdot, \sigma^2) : \mathbb{R}^N \rightarrow \mathbb{R}^{N \times N}$ parameterized by ϕ with the following score matching objective:

$$\min_{\phi} \mathbb{E}_{p(\tilde{\mathbf{x}})} \left[\left\| \mathcal{S}_\phi(\tilde{\mathbf{x}}, \sigma^2) - \nabla_{\tilde{\mathbf{x}}}^2 \log p(\tilde{\mathbf{x}}) \right\|_F^2 \right]. \quad (17)$$

The second-order score matching objective also has an equivalent denoising score matching formulation [29]:

$$\min_{\phi} \mathbb{E}_{p(\mathbf{x})p(\tilde{\mathbf{x}}|\mathbf{x})} \left[\left\| \mathcal{S}_\phi(\tilde{\mathbf{x}}, \sigma^2) - \mathbf{b}(\mathbf{x}, \tilde{\mathbf{x}}, \sigma^2) \mathbf{b}(\mathbf{x}, \tilde{\mathbf{x}}, \sigma^2)^\top + \frac{\mathbf{I}}{\sigma^2} \right\|_F^2 \right], \quad (18)$$

where $\mathbf{b}(\mathbf{x}, \tilde{\mathbf{x}}, \sigma^2) \triangleq \nabla_{\tilde{\mathbf{x}}} \log p(\tilde{\mathbf{x}}) + \frac{\tilde{\mathbf{x}} - \mathbf{x}}{\sigma^2}$. The objective in (18) relies on the ground-truth of the first-order score function, which is in general not accessible. In practice, we replace $\nabla_{\tilde{\mathbf{x}}} \log p(\tilde{\mathbf{x}})$ by the learned $\mathbf{s}_\theta(\tilde{\mathbf{x}}, \sigma^2)$ for efficient computation. The objective in (18) then becomes

$$\min_{\phi} \mathbb{E}_{p(\mathbf{x})p(\tilde{\mathbf{x}}|\mathbf{x})} \left[\left\| \mathcal{S}_\phi(\tilde{\mathbf{x}}, \sigma^2) - \hat{\mathbf{b}}(\mathbf{x}, \tilde{\mathbf{x}}, \sigma^2) \hat{\mathbf{b}}(\mathbf{x}, \tilde{\mathbf{x}}, \sigma^2)^\top + \frac{\mathbf{I}}{\sigma^2} \right\|_F^2 \right], \quad (19)$$

where $\hat{\mathbf{b}}(\mathbf{x}, \tilde{\mathbf{x}}, \sigma^2) \triangleq \mathbf{s}_\theta(\tilde{\mathbf{x}}, \sigma^2) + \frac{\tilde{\mathbf{x}} - \mathbf{x}}{\sigma^2}$. It is proved in [29] that with this replacement, the second-order score model has the error-bounded property if the first-order score matching error is bounded.

As in Line 11 of Algorithm 1, only the trace of the posterior covariance matrix is needed, rather than the covariance matrix itself. By noting in (12) the simple relation between the posterior covariance matrix and the second-order score function, it suffices to only match the trace of the second-order score function for posterior variance evaluation. The simplified objective is expressed as

$$\min_{\phi} \ell_2(\phi; \sigma) \triangleq \mathbb{E}_{p(\mathbf{x})p(\tilde{\mathbf{x}}|\mathbf{x})} \left[\left| \text{tr}(\mathcal{S}_\phi(\tilde{\mathbf{x}}, \sigma^2)) - \left\| \hat{\mathbf{b}}(\mathbf{x}, \tilde{\mathbf{x}}, \sigma^2) \right\|_2^2 + \frac{N}{\sigma^2} \right| \right]. \quad (20)$$

We combine (20) for all $\sigma \in \{\sigma_i\}_{i=1}^L$ to obtain the following unified objective for training the second-order score model:

$$\min_{\phi} \mathcal{L}_2(\phi; \{\sigma_i\}_{i=1}^L) \triangleq \frac{1}{L} \sum_{i=1}^L \lambda_2(\sigma_i) \ell_2(\phi; \sigma_i), \quad (21)$$

where $\lambda_2(\sigma_i)$ is the weighting factor depending on σ_i . In practice, one can first train a first-order score model, and then freeze it when applied to second-order score learning. Alternatively, the two score models can be trained both at once by disabling gradient backpropagation from the second-order training objective (21) to the first-order score model.

Algorithm 2: STMP Algorithm

```

1: Input:  $\mathbf{A}$ ,  $\mathbf{y}$ ,  $\delta_0^2$ ,  $\mathbf{x}_A^{\text{pri}}$ ,  $v_A^{\text{pri}}$ 
2: Output:  $\mathbf{x}_B^{\text{post}}$ 
3: repeat
4:   % LMMSE estimator (module A)
5:    $\mathbf{x}_A^{\text{post}} = \mathbf{x}_A^{\text{pri}} + \frac{v_A^{\text{pri}}}{v_A^{\text{pri}} + \delta_0^2} \mathbf{A}^\top (\mathbf{y} - \mathbf{A} \mathbf{x}_A^{\text{pri}})$ 
6:    $v_A^{\text{post}} = v_A^{\text{pri}} - \frac{M}{N} \frac{(v_A^{\text{pri}})^2}{v_A^{\text{pri}} + \delta_0^2}$ 
7:    $v_A^{\text{ext}} = \left( \frac{1}{v_A^{\text{post}}} - \frac{1}{v_A^{\text{pri}}} \right)^{-1}$ 
8:    $\mathbf{x}_A^{\text{ext}} = v_A^{\text{ext}} \left( \frac{\mathbf{x}_A^{\text{post}}}{v_A^{\text{post}}} - \frac{\mathbf{x}_A^{\text{pri}}}{v_A^{\text{pri}}} \right)$ 
9:    $\mathbf{x}_B^{\text{pri}} = \mathbf{x}_A^{\text{ext}}$ ,  $v_B^{\text{pri}} = v_A^{\text{ext}}$ 
10:  % Score-based MMSE denoiser (module B)
11:   $\mathbf{x}_B^{\text{post}} = \mathbf{x}_B^{\text{pri}} + v_B^{\text{pri}} \mathbf{s}_\theta(\mathbf{x}_B^{\text{pri}}, v_B^{\text{pri}})$ 
12:   $v_B^{\text{post}} = v_B^{\text{pri}} + \frac{(v_B^{\text{pri}})^2}{N} \text{tr}(\mathcal{S}_\phi(\mathbf{x}_B^{\text{pri}}, v_B^{\text{pri}}))$ 
13:   $v_B^{\text{ext}} = \left( \frac{1}{v_B^{\text{post}}} - \frac{1}{v_B^{\text{pri}}} \right)^{-1}$ 
14:   $\mathbf{x}_B^{\text{ext}} = v_B^{\text{ext}} \left( \frac{\mathbf{x}_B^{\text{post}}}{v_B^{\text{post}}} - \frac{\mathbf{x}_B^{\text{pri}}}{v_B^{\text{pri}}} \right)$ 
15:   $\mathbf{x}_A^{\text{pri}} = \mathbf{x}_B^{\text{ext}}$ ,  $v_A^{\text{pri}} = v_B^{\text{ext}}$ 
16: until the stopping criterion is met

```

V. STMP ALGORITHM

A. Overall Algorithm

The learned score models can be plugged into the TMP framework, facilitating MMSE denoising via

$$\mathbf{x}_B^{\text{post}} = \mathbf{x}_B^{\text{pri}} + v_B^{\text{pri}} \mathbf{s}_\theta(\mathbf{x}_B^{\text{pri}}, v_B^{\text{pri}}), \quad (22)$$

$$v_B^{\text{post}} = v_B^{\text{pri}} + \frac{(v_B^{\text{pri}})^2}{N} \text{tr}(\mathcal{S}_\phi(\mathbf{x}_B^{\text{pri}}, v_B^{\text{pri}})). \quad (23)$$

This score-based implementation yields the STMP algorithm summarized in Algorithm 2. An illustrative diagram is shown in Fig. 2. The iteration proceeds until either a preset maximum number of iterations is reached or the change in $\mathbf{x}_B^{\text{post}}$ across iterations falls below a predefined threshold. We have empirically observed that when the sampling ratio M/N is low, adding damping to the message updates helps to stabilize convergence. In particular, we suggest to replace Line 9 of Algorithm 2 by

$$\mathbf{x}_B^{\text{pri}} = \beta \mathbf{x}_A^{\text{ext}} + (1 - \beta) \mathbf{x}_{A, \text{old}}^{\text{ext}}, \quad (24)$$

$$v_B^{\text{pri}} = \beta v_A^{\text{ext}} + (1 - \beta) v_{A, \text{old}}^{\text{ext}}, \quad (25)$$

where $\mathbf{x}_{A, \text{old}}^{\text{ext}}$ and $v_{A, \text{old}}^{\text{ext}}$ are the extrinsic mean and variance of module A from the last iteration, and $\beta \in (0, 1]$ denotes the damping factor. Line 15 of Algorithm 2 should be modified similarly.

Remark 1. *There exist several alternative approaches for calculating the posterior variance v_B^{post} , such as residual-based variance estimation and Monte-Carlo divergence estimation. The former approach relies on the assumption that the denoiser output admits the decomposition*

$$\mathbf{x}_B^{\text{post}} = \mathbf{x} + \mathcal{N}(\mathbf{0}, v_B^{\text{post}} \mathbf{I}), \quad (26)$$

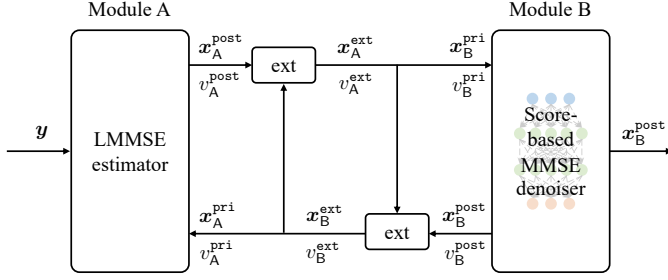


Fig. 2. Diagram the STMP algorithm.

where the effective denoising error is assumed to be Gaussian and independent of the measurement noise \mathbf{n} . Under this assumption, one may form an unbiased estimate of the variance as

$$v_B^{\text{post}} = \frac{\|\mathbf{y} - \mathbf{A}\mathbf{x}_B^{\text{post}}\|_2^2 - M\delta_0^2}{\|\mathbf{A}\|_F^2}. \quad (27)$$

However, these Gaussianity and independence assumptions rarely hold for practical denoisers, making this estimate unreliable. Another option is to approximate the average Jacobian trace of the denoiser via Monte Carlo sampling. Let $\boldsymbol{\varepsilon} \sim \mathcal{N}(\mathbf{0}, \mathbf{I})$ and define

$$\mathbf{x}_\delta^{\text{pri}} = \mathbf{x}_B^{\text{pri}} + \delta\boldsymbol{\varepsilon}, \quad (28)$$

$$\mathbf{x}_\delta^{\text{post}} = \mathbf{x}_\delta^{\text{pri}} + v_B^{\text{pri}} \mathbf{s}_\theta(\mathbf{x}_\delta^{\text{pri}}, v_B^{\text{pri}}). \quad (29)$$

With K Monte Carlo samples, the divergence is estimated as

$$\alpha = \frac{1}{NK} \sum_{k=1}^K \frac{((\mathbf{x}_\delta^{\text{post}})^{(k)} - (\mathbf{x}_B^{\text{post}})^{(k)})^\top \boldsymbol{\varepsilon}^{(k)}}{\delta}, \quad (30)$$

which yields the variance estimate

$$v_B^{\text{post}} = \alpha v_B^{\text{pri}}. \quad (31)$$

While this method is theoretically grounded, it introduces K additional denoiser evaluations, and may suffer from numerical instability for small δ .

B. State Evolution

The asymptotic MSE performance of STMP can be accurately predicted by a set of SE equations. We begin by defining the following MSE function, which describes the denoising performance of the score-based denoiser under an AWGN model:

$$\text{MSE}(v) \triangleq \frac{1}{N} \mathbb{E} \left[\|\mathbf{r} + v\mathbf{s}_\theta(\mathbf{r}, v) - \mathbf{x}\|_2^2 \right], \quad (32)$$

$$\mathbf{r} = \mathbf{x} + \mathcal{N}(\mathbf{0}, v\mathbf{I}), \quad (33)$$

where \mathbf{r} denotes the denoiser input, and $\mathbf{r} + v\mathbf{s}_\theta(\mathbf{r}, v)$ is the posterior mean estimate produced via Tweedie's formula. The average posterior variance of the denoiser satisfies

$$v_B^{\text{post}} = \mathbb{E} \left[\frac{1}{N} \sum_{n=1}^N \text{Var}[x_n | \mathbf{x}_B^{\text{pri}}] \right] = \text{MSE}(v_B^{\text{pri}}), \quad (34)$$

where v_B^{pri} denotes the average prior variance entering the denoiser. In the large-system limit, where the problem dimension tends to infinity with a fixed sampling ratio M/N , the

evolution of STMP is described by the following SE recursion for v_A^{pri} and v_B^{pri} [6]:

$$v_B^{\text{pri}} = \frac{N}{M} (v_A^{\text{pri}} + \delta_0^2) - v_A^{\text{pri}}, \quad (35)$$

$$v_A^{\text{pri}} = \left(\frac{1}{\text{MSE}(v_B^{\text{pri}})} - \frac{1}{v_B^{\text{pri}}} \right)^{-1}. \quad (36)$$

Eqn. (35) follows from the updates in Lines 6, 7, and 9 of Algorithm 2. Similarly, Eqn. (36) follows from the updates in Lines 13 and 15 of Algorithm 2. We initialize the SE recursion with $v_A^{\text{pri}}(0) = \mathbb{E}[\|\mathbf{x}\|_2^2]/N$. At iteration t , the asymptotic MSE of STMP is then predicted by $\text{MSE}(v_B^{\text{pri}}(t))$. Notably, the fixed points of the above SE equations coincide with the Bayes-optimal MSE predicted by the replica method [7].

Remark 2. A practical consideration in evaluating the SE equations is that the MSE function of the denoiser defined in (32) does not admit a closed-form expression. Its value must be obtained numerically by invoking the score-based denoiser at different noise levels, which can be computationally expensive or even infeasible during SE evaluation. To avoid repeatedly executing the denoiser inside the SE recursion, one may precompute a lookup table that maps each prior variance v to its corresponding posterior variance $\text{MSE}(v)$. The resulting discrete mapping can then be interpolated to obtain a continuous approximation of $\text{MSE}(v)$ over the relevant range of variances.

VI. EXTENSION TO QUANTIZED COMPRESSIVE IMAGING

Due to the finite precision of ADCs and constraints on data storage, measurements in compressive imaging are often quantized. This section generalizes STMP to quantized systems and derives the corresponding SE equations to characterize its asymptotic performance.

A. Problem Statement

Quantized compressive imaging aims to reconstruct an unknown signal $\mathbf{x} \in \mathbb{R}^N$ from quantized and noisy measurements $\mathbf{y} \in \mathcal{Q}^M$, given by

$$\mathbf{y} = \mathbf{Q}(\mathbf{z} + \mathbf{n}), \quad \mathbf{z} = \mathbf{A}\mathbf{x}, \quad (37)$$

where $\mathbf{Q}(\cdot) : \mathbb{R}^M \rightarrow \mathcal{Q}^M$ is an element-wise quantization operator. Specifically, each scalar component $y_m = \mathbf{Q}(z_m + n_m)$ is mapped to one of the 2^B quantization levels contained in the discrete codebook \mathcal{Q} , where B denotes the quantization bit depth. The quantizer partitions the real line into 2^B contiguous intervals:

$$(-\infty, r_1], (r_1, r_2], \dots, (r_{2^B-1}, \infty), \quad (38)$$

where $\{r_b\}_{b=0}^{2^B}$ are the decision thresholds with $r_0 = -\infty$ and $r_{2^B} = \infty$. For a uniform mid-rise quantizer, the thresholds are evenly spaced with the quantization interval $\Delta > 0$, given by $r_b = (b - 2^{B-1})\Delta$ for $b = 1, 2, \dots, 2^B - 1$. The output of the quantizer is then assigned as

$$y_m = r_b - \frac{\Delta}{2}, \quad \text{if } z_m + n_m \in (r_{b-1}, r_b]. \quad (39)$$

When $B = 1$, the model reduces to 1-bit quantized compressive sensing with binary measurements.

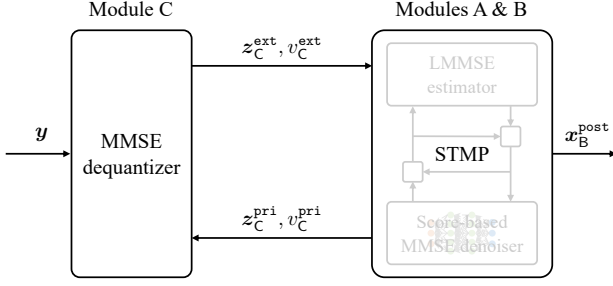


Fig. 3. Diagram of the Q-STMP algorithm.

B. Q-STMP Algorithm

The proposed extension draws inspiration from EP [30] and its application to GLMs [31]. As shown in Fig. 3, the key idea is to integrate the original STMP algorithm with an additional dequantization module (module C) in a turbo manner [51]. Module C performs component-wise MMSE estimation of z based on the quantization likelihood $p(\mathbf{y}|\mathbf{z}) = \prod_{m=1}^M p(y_m|z_m)$ and a Gaussian pseudo-prior $\mathcal{N}(z; z_C^{\text{pri}}, v_C^{\text{pri}} \mathbf{I})$. Then, it produces an extrinsic estimate of z , which is modeled as

$$z_C^{\text{ext}} = \mathbf{A}\mathbf{x} + \mathbf{n}_C^{\text{ext}}, \text{ with } \mathbf{n}_C^{\text{ext}} \sim \mathcal{N}(\mathbf{0}, v_C^{\text{ext}} \mathbf{I}), \quad (40)$$

where z_C^{ext} and v_C^{ext} represent the effective linear measurements and noise variance after dequantization. These pseudo-measurements are then fed into the STMP algorithm to update the belief on \mathbf{x} and consequently refine the prior of $z = \mathbf{A}\mathbf{x}$ provided to module C. The algorithm iterates between module C and the STMP block (modules A and B), progressively improving both the dequantized signal estimate and the reconstructed image.

Specifically, we initialize the prior mean and variance for module C as $\mathcal{N}(z; z_C^{\text{pri}}, v_C^{\text{pri}} \mathbf{I})$. For each scalar entry z_m , the posterior mean and variance are given by the component-wise MMSE estimator:

$$z_{C,m}^{\text{post}} = \mathbb{E}[z_m | z_{C,m}^{\text{pri}}], \quad (41)$$

$$v_{C,m}^{\text{post}} = \text{Var}[z_m | z_{C,m}^{\text{pri}}], \quad (42)$$

where the expectation is taken with respect to (w.r.t.) the posterior distribution

$$p(z_m | y_m) \propto p(y_m | z_m) \mathcal{N}(z_m; z_{C,m}^{\text{pri}}, v_C^{\text{pri}}). \quad (43)$$

For the considered quantization model, measurement y_m indicates that the noisy observation satisfies $z_m + n_m \in (r_{b_m-1}, r_{b_m}]$. Equivalently, conditioned on z_m , the likelihood is the probability that a Gaussian random variable with mean z_m and variance δ_0^2 falls inside this interval, i.e.,

$$p(y_m | z_m) = \Phi\left(\frac{r_{b_m} - z_m}{\delta_0}\right) - \Phi\left(\frac{r_{b_m-1} - z_m}{\delta_0}\right), \quad (44)$$

where $\Phi(x) \triangleq (1/\sqrt{2\pi}) \int_{-\infty}^x e^{-t^2/2} dt$ denotes the cumulative distribution function (CDF) of standard normal distribution. Therefore, the product in (43) is proportional to a Gaussian

Algorithm 3: Q-STMP Algorithm

```

1: Input:  $\mathbf{A}, \mathbf{y}, \delta_0^2, \mathbf{x}_A^{\text{pri}}, v_A^{\text{pri}}$ 
2: Output:  $\mathbf{x}_B^{\text{post}}$ 
3:  $z_C^{\text{pri}} = \mathbf{A}\mathbf{x}_A^{\text{pri}}, v_C^{\text{pri}} = v_A^{\text{pri}}$ 
4: repeat
5:   % MMSE dequantizer (module C)
6:    $z_{C,m}^{\text{post}} = z_{C,m}^{\text{pri}} - \frac{v_C^{\text{pri}}}{\sqrt{v_C^{\text{pri}} + \delta_0^2}} \frac{\phi(\eta_m^u) - \phi(\eta_m^l)}{\Phi(\eta_m^u) - \Phi(\eta_m^l)}, \forall m$ 
7:    $v_C^{\text{post}} = v_C^{\text{pri}} - \frac{(v_C^{\text{pri}})^2}{M(v_C^{\text{pri}} + \delta_0^2)} \sum_{m=1}^M \left( \frac{\eta_m^u \phi(\eta_m^u) - \eta_m^l \phi(\eta_m^l)}{\Phi(\eta_m^u) - \Phi(\eta_m^l)} + \left( \frac{\phi(\eta_m^u) - \phi(\eta_m^l)}{\Phi(\eta_m^u) - \Phi(\eta_m^l)} \right)^2 \right)$ 
8:    $v_C^{\text{ext}} = \left( \frac{1}{v_C^{\text{post}}} - \frac{1}{v_C^{\text{pri}}} \right)^{-1}$ 
9:    $z_C^{\text{ext}} = v_C^{\text{ext}} \left( \frac{z_C^{\text{post}}}{v_C^{\text{post}}} - \frac{z_C^{\text{pri}}}{v_C^{\text{pri}}} \right)$ 
10:  % LMMSE estimator (module A)
11:   $\mathbf{x}_A^{\text{post}} = \mathbf{x}_A^{\text{pri}} + \frac{v_A^{\text{pri}}}{v_A^{\text{pri}} + v_C^{\text{ext}}} \mathbf{A}^\top (z_C^{\text{ext}} - \mathbf{A}\mathbf{x}_A^{\text{pri}})$ 
12:   $v_A^{\text{post}} = v_A^{\text{pri}} - \frac{M}{N} \frac{(v_A^{\text{pri}})^2}{v_A^{\text{pri}} + v_C^{\text{ext}}}$ 
13:   $v_B^{\text{pri}} = v_B^{\text{ext}} = \left( \frac{1}{v_A^{\text{post}}} - \frac{1}{v_A^{\text{pri}}} \right)^{-1}$ 
14:   $\mathbf{x}_B^{\text{pri}} = \mathbf{x}_A^{\text{ext}} = v_A^{\text{ext}} \left( \frac{\mathbf{x}_A^{\text{post}}}{v_A^{\text{post}}} - \frac{\mathbf{x}_A^{\text{pri}}}{v_A^{\text{pri}}} \right)$ 
15:  % Score-based MMSE denoiser (module B)
16:   $\mathbf{x}_B^{\text{post}} = \mathbf{x}_B^{\text{pri}} + v_B^{\text{pri}} \mathbf{s}_\theta(\mathbf{x}_B^{\text{pri}}, v_B^{\text{pri}})$ 
17:   $v_B^{\text{post}} = v_B^{\text{pri}} + \frac{(v_B^{\text{pri}})^2}{N} \text{tr}(\mathbf{S}_\theta(\mathbf{x}_B^{\text{pri}}, v_B^{\text{pri}}))$ 
18:   $v_A^{\text{pri}} = v_B^{\text{ext}} = \left( \frac{1}{v_B^{\text{post}}} - \frac{1}{v_B^{\text{pri}}} \right)^{-1}$ 
19:   $\mathbf{x}_A^{\text{pri}} = \mathbf{x}_B^{\text{ext}} = v_B^{\text{ext}} \left( \frac{\mathbf{x}_B^{\text{post}}}{v_B^{\text{post}}} - \frac{\mathbf{x}_B^{\text{pri}}}{v_B^{\text{pri}}} \right)$ 
20:   $z_C^{\text{pri}} = \mathbf{A}\mathbf{x}_A^{\text{pri}}, v_C^{\text{pri}} = v_A^{\text{pri}}$ 
21: until the stopping criterion is met

```

distribution truncated to a normalized interval. Define the normalized truncation bounds:

$$\eta_m^u \triangleq \frac{r_{b_m} - z_{C,m}^{\text{pri}}}{\sqrt{v_C^{\text{pri}} + \delta_0^2}}, \quad \eta_m^l \triangleq \frac{r_{b_m-1} - z_{C,m}^{\text{pri}}}{\sqrt{v_C^{\text{pri}} + \delta_0^2}}. \quad (45)$$

Denote the PDF of standard normal distribution by $\phi(x) \triangleq (1/\sqrt{2\pi})e^{-x^2/2}$. Using standard identities for truncated Gaussian distributions [47], the posterior mean and variance becomes

$$\begin{aligned} z_{C,m}^{\text{post}} &= \frac{\int z_m p(y_m | z_m) \mathcal{N}(z_m; z_{C,m}^{\text{pri}}, v_C^{\text{pri}}) dz_m}{\int p(y_m | z_m) \mathcal{N}(z_m; z_{C,m}^{\text{pri}}, v_C^{\text{pri}}) dz_m} \\ &= z_{C,m}^{\text{pri}} - \frac{v_C^{\text{pri}}}{\sqrt{v_C^{\text{pri}} + \delta_0^2}} \frac{\phi(\eta_m^u) - \phi(\eta_m^l)}{\Phi(\eta_m^u) - \Phi(\eta_m^l)}, \end{aligned} \quad (46)$$

$$\begin{aligned} v_{C,m}^{\text{post}} &= \frac{\int (z_m - z_{C,m}^{\text{post}})^2 p(y_m | z_m) \mathcal{N}(z_m; z_{C,m}^{\text{pri}}, v_C^{\text{pri}}) dz_m}{\int p(y_m | z_m) \mathcal{N}(z_m; z_{C,m}^{\text{pri}}, v_C^{\text{pri}}) dz_m} \\ &= v_C^{\text{pri}} - \frac{(v_C^{\text{pri}})^2}{v_C^{\text{pri}} + \delta_0^2} \left(\frac{\eta_m^u \phi(\eta_m^u) - \eta_m^l \phi(\eta_m^l)}{\Phi(\eta_m^u) - \Phi(\eta_m^l)} + \left(\frac{\phi(\eta_m^u) - \phi(\eta_m^l)}{\Phi(\eta_m^u) - \Phi(\eta_m^l)} \right)^2 \right). \end{aligned} \quad (47)$$

The posterior variance from module C is averaged over all dimensions as

$$v_C^{\text{post}} = \frac{1}{M} \sum_{m=1}^M v_{C,m}^{\text{post}}. \quad (48)$$

The corresponding extrinsic variance and mean are respectively given by

$$v_C^{\text{ext}} = \left(\frac{1}{v_C^{\text{post}}} - \frac{1}{v_C^{\text{pri}}} \right)^{-1}, \quad (49)$$

$$z_C^{\text{ext}} = v_C^{\text{ext}} \left(\frac{z_C^{\text{post}}}{v_C^{\text{post}}} - \frac{z_C^{\text{pri}}}{v_C^{\text{pri}}} \right). \quad (50)$$

The extrinsic output is then used as the pseudo measurement in (40) and fed into the STMP block. Within modules A and B, one or multiple STMP iterations may be executed before passing updated messages back to module C. Specifically, the STMP block produces x_B^{ext} and v_B^{ext} , from which the prior for the next module-C update is constructed as $z_C^{\text{pri}} = \mathbf{A}x_B^{\text{ext}}$, and $v_C^{\text{pri}} = \text{tr}(v_B^{\text{ext}} \mathbf{A} \mathbf{A}^\top) / M = v_B^{\text{ext}}$. The complete procedures are summarized in Algorithm 3.

C. State Evolution

In the large-system limit, the empirical average in (48) concentrates around its ensemble expectation, allowing v_C^{post} to be expressed as an expectation w.r.t. the joint distribution $p(z_C^{\text{pri}}, y)$. As all measurement components are statistically identical in this limit, the component index m is dropped hereafter. The resulting transfer function that characterizes the prior-to-posterior variance mapping of module C is given by

$$v_C^{\text{post}} = v_C^{\text{pri}} - \frac{(v_C^{\text{pri}})^2}{v_C^{\text{pri}} + \delta_0^2} \mathbb{E}_{p(z_C^{\text{pri}}, y)} \left[\frac{\eta^\mu \phi(\eta^\mu) - \eta^\eta \phi(\eta^\eta)}{\Phi(\eta^\mu) - \Phi(\eta^\eta)} + \left(\frac{\phi(\eta^\mu) - \phi(\eta^\eta)}{\Phi(\eta^\mu) - \Phi(\eta^\eta)} \right)^2 \right] \quad (51)$$

$$= v_C^{\text{pri}} - (v_C^{\text{pri}})^2 \mathbb{E}_{p(z_C^{\text{pri}}, y)} \left[- \frac{\Psi''(y; z_C^{\text{pri}}, v_C^{\text{pri}} + \delta_0^2)}{\Psi(y; z_C^{\text{pri}}, v_C^{\text{pri}} + \delta_0^2)} + \left(\frac{\Psi'(y; z_C^{\text{pri}}, v_C^{\text{pri}} + \delta_0^2)}{\Psi(y; z_C^{\text{pri}}, v_C^{\text{pri}} + \delta_0^2)} \right)^2 \right], \quad (52)$$

where

$$\Psi(y; z_C^{\text{pri}}, v_C^{\text{pri}} + \delta_0^2) \triangleq \Phi(\eta^\mu) - \Phi(\eta^\eta), \quad (53)$$

$$\Psi'(y; z_C^{\text{pri}}, v_C^{\text{pri}} + \delta_0^2) = - \frac{\phi(\eta^\mu) - \phi(\eta^\eta)}{\sqrt{v_C^{\text{pri}} + \delta_0^2}}, \quad (54)$$

$$\Psi''(y; z_C^{\text{pri}}, v_C^{\text{pri}} + \delta_0^2) = - \frac{\eta^\mu \phi(\eta^\mu) - \eta^\eta \phi(\eta^\eta)}{v_C^{\text{pri}} + \delta_0^2}. \quad (55)$$

The joint distribution of z_C^{pri} and y follows from [47] as

$$p(z_C^{\text{pri}}, y) = \mathcal{N}(z_C^{\text{pri}}; 0, v_z - v_C^{\text{pri}}) \Psi(y; z_C^{\text{pri}}, v_C^{\text{pri}} + \delta_0^2), \quad (56)$$

where $v_z = \sum_{m=1}^M \mathbb{E}[|z_m|^2] / M$. The expectation in (51) can thus be written as an integral over the standard Gaussian

measure $Dz = (1/\sqrt{2\pi})e^{-z^2/2}dz$. Since the first term inside the expectation evaluates to zero, we obtain

$$v_C^{\text{post}} = v_C^{\text{pri}} - (v_C^{\text{pri}})^2 \times \underbrace{\sum_{y \in \mathcal{Q}} \int Dz \frac{(\Psi'(y; \sqrt{v_z - v_C^{\text{pri}}} z, v_C^{\text{pri}} + \delta_0^2))^2}{\Psi(y; \sqrt{v_z - v_C^{\text{pri}}} z, v_C^{\text{pri}} + \delta_0^2)}}_{\triangleq \vartheta(v_C^{\text{pri}})}. \quad (57)$$

Substituting (57) into (49) gives the extrinsic variance passed from module C to module A:

$$v_C^{\text{ext}} = \vartheta^{-1}(v_C^{\text{pri}}) - v_C^{\text{pri}}. \quad (58)$$

Finally, substituting (58) into the variance recursions of modules A and B, and using the identity $v_C^{\text{pri}} = v_A^{\text{pri}}$, we obtain the SE of Q-STMP in the following scalar form:

$$\vartheta(v_A^{\text{pri}}) = \sum_{y \in \mathcal{Q}} \int Dz \frac{(\Psi'(y; \sqrt{v_z - v_A^{\text{pri}}} z, v_A^{\text{pri}} + \delta_0^2))^2}{\Psi(y; \sqrt{v_z - v_A^{\text{pri}}} z, v_A^{\text{pri}} + \delta_0^2)}, \quad (59)$$

$$v_B^{\text{pri}} = \frac{N}{M} \vartheta^{-1}(v_A^{\text{pri}}) - v_A^{\text{pri}}, \quad (60)$$

$$v_A^{\text{pri}} = \left(\frac{1}{\text{MSE}(v_B^{\text{pri}})} - \frac{1}{v_B^{\text{pri}}} \right)^{-1}. \quad (61)$$

VII. EXPERIMENTS

In this section, we evaluate the performance of the proposed methods on the FFHQ 256×256 dataset [32]. We adopt the pre-trained score function in [17] as our first-order score model. Unfortunately, there is no publicly available second-order score model on the FFHQ dataset. For training the second-order score model, we adopt the NCSN++ architecture [17] that outputs only the diagonal value of the second-order score, yielding the same output dimension as the first-order score model. The focus on the diagonal is due to the fact that only the trace of the second-order score is pertinent to the posterior variance evaluation. The training of the second-order score model follows the same default settings as its first-order counterpart [17]. For inference, we test our proposed method and several benchmarks on 1000 images from the validation set of the FFHQ dataset. The measurement matrix takes the form of $\mathbf{A} = \mathbf{S} \mathbf{W} \mathbf{\Theta}$, where $\mathbf{S} \in \mathbb{R}^{M \times N}$ is a random row selection matrix consisting of randomly selected rows from a permutation matrix, $\mathbf{W} \in \mathbb{R}^{N \times N}$ is a DCT matrix, and $\mathbf{\Theta} \in \mathbb{R}^{N \times N}$ is a diagonal matrix with random signs (1 or -1) in the diagonal.

A. Results on Compressive Image Recovery

We compare the proposed STMP algorithm against both state-of-the-art score-based posterior sampling techniques and traditional PnP methods. The baselines include:

- **DPS** [24]: We follow the original paper and use 1000 reverse-diffusion steps, with the parameter ζ set to 1.
- **DiffPIR** [26]: We follow the original paper and use 100 reverse-diffusion steps, with the parameters (λ, ζ) set to (5, 1).

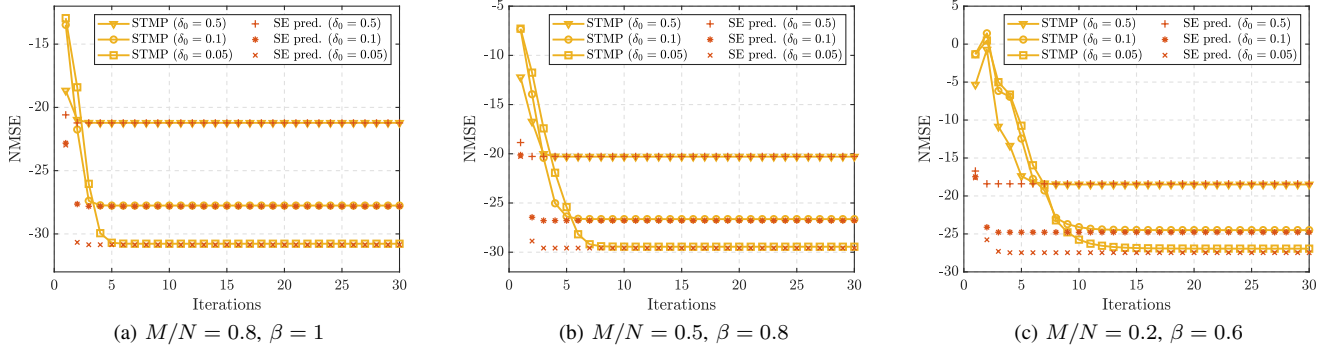


Fig. 4. Convergence behaviors and SE predictions of STMP for different sampling ratios and noise levels.

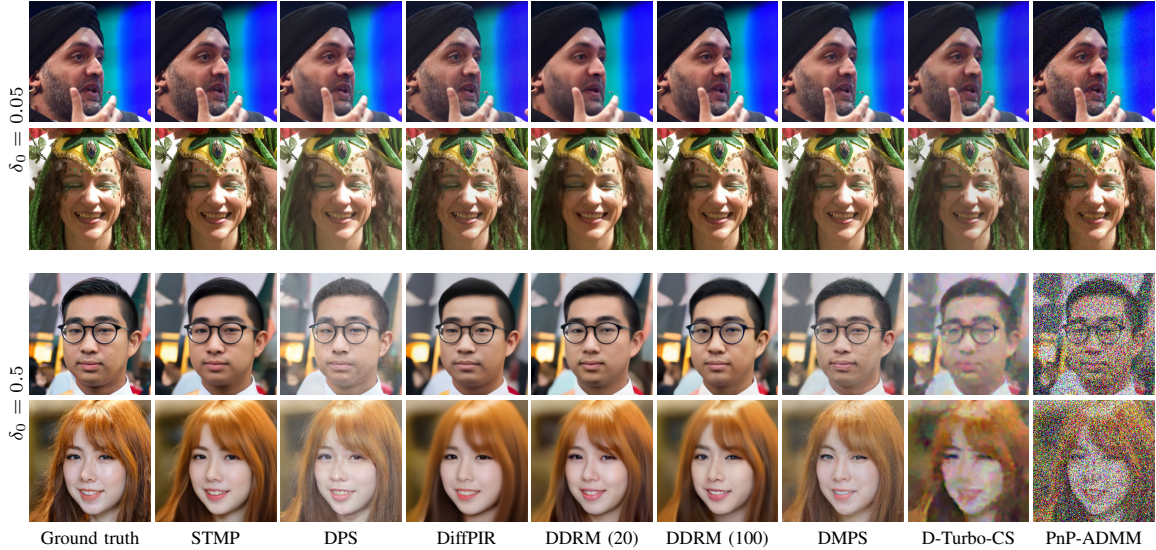


Fig. 5. Representative results for compressive image recovery on the FFHQ validation set. The sampling ratio is $M/N = 0.7$ and we set $\beta = 1$ for STMP.

- **DDRM [22]**: We use both 20 and 100 reverse-diffusion steps. The parameters (η, η_b) are set to $(0.85, 1)$.
- **DMPS [21]**: We follow the original paper and use 1000 reverse-diffusion steps, with the parameter λ set to 1.75.
- **D-Turbo-CS [10]**: We choose the BM3D denoiser for D-Turbo-CS. The algorithm is executed for 50 iterations.
- **PnP-ADMM [34]**: We choose the TV denoiser for PnP-ADMM and the parameters (λ, ρ, γ) are set to $(0.01, 1, 1)$. The algorithm is executed for 50 iterations.

Fig. 4 shows the normalized MSE (NMSE) trajectory of the reconstruction throughout the iterations of STMP. Overall, the proposed algorithm exhibits fast convergence (typically less than 10 iterations) across a wide range of sampling ratios and noise levels. As expected, the number of iterations required for convergence increases as the sampling ratio M/N decreases, since recovering an image from fewer measurements becomes more ill-posed. In addition, the algorithm converges slightly more slowly when the measurement noise is small. Regarding the SE characterization, we observe that the SE equations provide highly accurate predictions of the converged NMSE achieved by STMP. This agreement confirms that SE precisely captures the asymptotic fixed-point behavior of the algorithm. However, before convergence, a noticeable mismatch arises between the SE prediction and the empirical performance. We conjecture that this discrepancy stems from practical

deviations of the denoiser’s input noise from the assumed AWGN model, as well as from score-matching errors in the learned first- and second-order score functions.

Figs. 5 and 6 present representative qualitative results for compressive image recovery at sampling ratios $M/N = 0.7$ and $M/N = 0.1$, respectively. When the sampling ratio is high, all score-based baselines, including STMP, DPS, DiffPIR, DDRM, and DMPS, produce visually high-quality reconstructions that preserve facial geometry and texture details. In contrast, the conventional PnP approaches D-Turbo-CS and PnP-ADMM, which rely on generic denoisers rather than learned score priors, struggle to produce satisfactory outputs and exhibit significant artifacts. When the sampling ratio is low, the differences between the methods become more pronounced. DDRM often produces samples that are inconsistent with the ground-truth measurement, yielding images that are visually plausible but unrelated to the underlying subject. DPS outperforms DDRM but still fails to remain faithful to the observations when the noise level is high. For instance, in the last row of Fig. 6, DPS reconstructs a man wearing transparent glasses, whereas the ground truth clearly shows sunglasses, indicating a hallucination caused by its stochastic sampling dynamics. This deviation highlights the superior fidelity of our proposed STMP method, which consistently adheres to the measurement across all noise levels and sampling ratios.

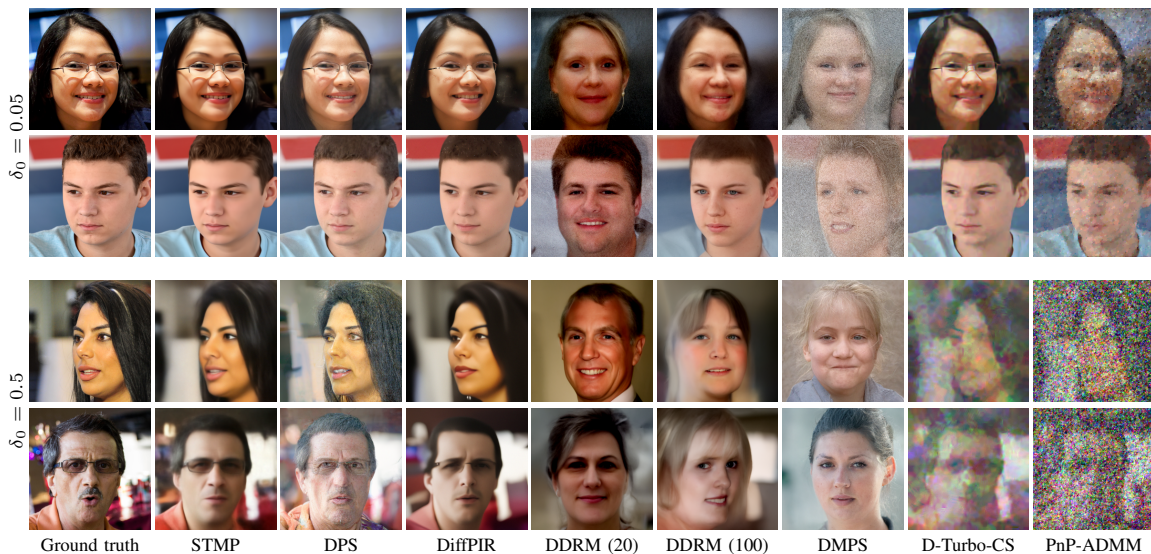


Fig. 6. Representative results for compressive image recovery on the FFHQ validation set. The sampling ratio is $M/N = 0.1$ and we set $\beta = 0.5$ for STMP.

TABLE I
QUANTITATIVE RESULTS FOR COMPRESSIVE IMAGE RECOVERY ON THE FFHQ VALIDATION SET (**BOLD**: BEST, UNDERLINE: SECOND BEST)

Compression ratio	Method	$\delta_0 = 0.5$				$\delta_0 = 0.05$			
		PSNR \uparrow	SSIM \uparrow	FID \downarrow	LPIPS \downarrow	PSNR \uparrow	SSIM \uparrow	FID \downarrow	LPIPS \downarrow
$M/N = 0.7$	STMP (Ours)	25.82	0.7649	57.76	0.2089	34.98	0.9420	<u>23.42</u>	<u>0.0437</u>
	DPS	17.98	0.5888	39.98	0.2323	28.33	0.8596	28.33	0.0857
	DiffPIR	24.19	0.7015	86.51	0.2870	28.05	0.7728	27.00	0.0914
	DDRM (20)	24.77	0.7252	58.90	0.2253	29.10	0.8552	37.92	0.1192
	DDRM (100)	<u>25.01</u>	<u>0.7339</u>	57.00	<u>0.2184</u>	<u>31.79</u>	<u>0.9108</u>	25.42	0.0636
	DMPS	18.68	0.5878	<u>48.32</u>	0.2383	30.14	0.8878	13.78	0.0341
	D-Turbo-CS	19.28	0.5390	146.73	0.5131	28.17	0.8715	37.09	0.1141
	PnP-ADMM	8.68	0.0400	341.78	1.4445	29.15	0.7314	43.26	0.1735
$M/N = 0.4$	STMP (Ours)	24.73	0.7320	61.22	0.2441	33.49	0.9249	31.35	0.0633
	DPS	16.75	0.5466	44.89	0.2632	26.66	0.8273	<u>26.46</u>	0.0971
	DiffPIR	23.18	0.6461	<u>59.82</u>	<u>0.2490</u>	28.23	0.8100	24.22	<u>0.0667</u>
	DDRM (20)	22.37	0.6527	68.61	0.2884	25.62	0.7673	42.79	0.1798
	DDRM (100)	<u>23.58</u>	<u>0.6850</u>	62.56	0.2578	<u>29.47</u>	<u>0.8599</u>	30.43	0.0995
	DMPS	16.66	0.5315	63.92	0.3130	25.73	0.7990	26.63	0.0986
	D-Turbo-CS	18.05	0.4883	204.67	0.5697	26.79	0.8378	42.84	0.1524
	PnP-ADMM	8.75	0.0381	352.42	1.4230	28.89	0.7530	56.15	0.1846
$M/N = 0.1$	STMP (Ours)	22.07	0.6447	<u>68.85</u>	0.3388	29.86	0.8615	<u>46.09</u>	0.1228
	DPS	14.01	0.4447	56.23	<u>0.3470</u>	22.15	0.7170	29.36	<u>0.1446</u>
	DiffPIR	<u>21.07</u>	<u>0.6149</u>	97.38	0.3572	<u>25.52</u>	<u>0.7539</u>	56.30	0.1622
	DDRM (20)	11.82	0.3286	95.36	0.5249	12.66	0.2819	122.80	0.6120
	DDRM (100)	18.48	0.5225	105.22	0.4188	21.43	0.6274	68.89	0.3072
	DMPS	11.31	0.3188	92.56	0.5561	12.31	0.1787	185.04	0.8939
	D-Turbo-CS	15.47	0.3913	291.16	0.6741	23.98	0.7324	63.58	0.2861
	PnP-ADMM	11.46	0.0638	374.52	1.0889	19.16	0.4646	310.09	0.5784

In Table I, we report the average peak signal-to-noise ratio (PSNR), structural similarity index measure (SSIM), Fréchet inception distance (FID), and learned perceptual image patch similarity (LPIPS) to assess fidelity to the ground-truth image and perceptual reconstruction quality. Across different sampling ratios and noise levels, the proposed STMP algorithm consistently outperforms competing baselines on the majority of these metrics. In particular, STMP achieves the highest PSNR and SSIM in all settings, indicating superior pixel-level accuracy and structural preservation. At the same time, its lower FID and LPIPS scores demonstrate that STMP also produces more realistic and perceptually convincing images. These results collectively show that STMP not only adheres closely to the underlying measurements but also delivers

highly competitive perceptual quality.

Fig. 7 illustrates the tradeoff between reconstruction performance and computational complexity. For the baseline algorithms, we generate the tradeoff curves by varying the number of reverse-diffusion steps, whereas for STMP we directly report the reconstruction performance at each iteration. Compared with DiffPIR, DPS, and DDRM, the proposed STMP algorithm achieves high SSIM and low LPIPS within only a small number of iterations, demonstrating its superior efficiency. Regarding per-iteration complexity, the computational cost of these methods is dominated by the NFEs of the score network. In STMP, each iteration requires one NFE from the first-order score network and one NFE from the second-order score network. However, these two NFEs can be

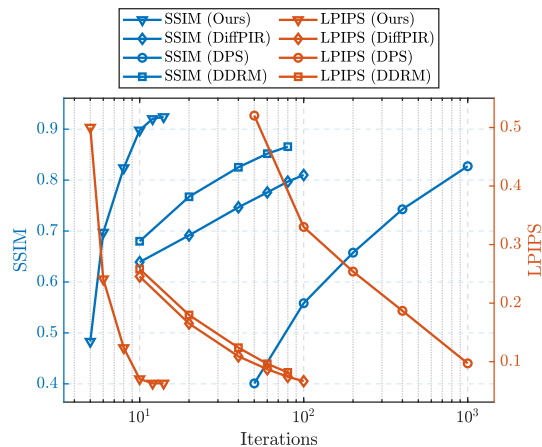


Fig. 7. Tradeoff between reconstruction faithfulness / perceptual image quality and computational complexity. The compression ratio is $M/N = 0.4$ and the noise level is $\delta_0 = 0.05$. We set $\beta = 0.8$ for STMP.

executed in parallel, meaning that the overall time per iteration is comparable to that of DiffPIR and DDRM, both of which involve only a single NFE per step. In contrast, DPS requires not only forward propagation during each NFE, but also backpropagating gradients through the score network. This makes the iterative steps in DPS even more computationally expensive.

B. Results on Quantized Compressive Image Recovery

In this subsection, we compare the Q-STMP algorithm with the following baselines:

- **QCS-SGM [48]:** We follow the original paper and use 2311 reverse-diffusion steps. We choose $\epsilon = 0.00005$ for the 1-bit setting, and $\epsilon = 0.00002$ for all higher-bit quantization levels.
- **GTurbo-SR [47]:** We choose the BM3D denoiser for D-Turbo-CS. The algorithm is executed for 50 iterations.

Fig. 8 shows the NMSE trajectories and corresponding SE predictions for Q-STMP under different sampling ratios and quantization bit depths. Similar to STMP, Q-STMP exhibits rapid convergence, and the converged performance aligns closely with the SE predictions. Notably, increasing the number of quantization bits from 1 to 3 yields only marginal improvements in reconstruction performance. This suggests that the FFHQ image data possess significant redundancy, allowing Q-STMP to recover meaningful image content even from extremely coarsely quantized observations.

Fig. 9 presents representative results for quantized compressive image recovery under different sampling ratios and quantization bit depths. Across all settings, Q-STMP consistently produces sharp and faithful reconstructions, even at extremely low bit levels such as 1 or 2 bits. In contrast, competing approaches including QCS-SGM and GTurbo-SR often introduce noticeable artifacts, oversmoothing, or hallucinated details, with degradation becoming more severe as the quantization becomes coarser. The robustness of Q-STMP to both low sampling ratios and aggressive quantization highlights the strong expressive power of the score-based generative prior and the effectiveness of the TMP and EP frameworks in

handling heavily distorted measurements. Table II summarizes the quantitative performance of all methods in terms of PSNR, SSIM, FID, and LPIPS.

Fig. 10 illustrates how the reconstruction quality of Q-STMP varies with the quantization bit depth. As the number of bits increases, both PSNR and LPIPS improve steadily, with notable gains from 1 to 4 bits and diminishing returns thereafter. Notably, Q-STMP already approaches the performance of STMP for unquantized systems even with moderate bit depths (4 to 6 bits), especially for the higher-noise setting $\delta_0 = 0.5$. These results highlight the robustness of Q-STMP to coarse quantization and demonstrate that only a small number of bits is sufficient to achieve near-optimal reconstruction fidelity.

VIII. CONCLUSIONS

In this paper, we introduced STMP, a novel approach for compressive image recovery using unconditional score networks. STMP inherits the fast convergence speed of message-passing algorithms and, meanwhile, takes full advantage of the expressive prior through the integration of score-based generative models. To deal with quantized measurements, we further proposed Q-STMP, which augments STMP with a component-wise MMSE dequantizer. We demonstrated that the asymptotic performance of STMP and Q-STMP can be accurately predicted by a set of SE equations. Experimental results on the FFHQ dataset highlight the efficiency and state-of-the-art performance of STMP and Q-STMP against a variety of benchmarks.

REFERENCES

- [1] C. Cai, X. Yuan, and Y.-J. A. Zhang, “Score-based turbo message passing for plug-and-play compressive image recovery,” in *Proc. IEEE Int. Workshop on Signal Process. Artif. Intell. Wireless Commun.*, 2025, pp. 1–5.
- [2] C. A. Metzler, A. Maleki, and R. G. Baraniuk, “From denoising to compressed sensing,” *IEEE Trans. Inf. Theory*, vol. 62, no. 9, pp. 5117–5144, 2016.
- [3] M. T. Vlaardingerbroek and J. A. Boer, *Magnetic resonance imaging: theory and practice*. Springer Science & Business Media, 2013.
- [4] A. Moreira, P. Prats-Iraola, M. Younis, G. Krieger, I. Hajnsek, and K. P. Papathanassiou, “A tutorial on synthetic aperture radar,” *IEEE Geosci. Remote Sens. Mag.*, vol. 1, no. 1, pp. 6–43, 2013.
- [5] T. M. Buzug, “Computed tomography,” in *Springer handbook of medical technology*. Springer, 2011, pp. 311–342.
- [6] J. Ma, X. Yuan, and L. Ping, “Turbo compressed sensing with partial DFT sensing matrix,” *IEEE Signal Process. Lett.*, vol. 22, no. 2, pp. 158–161, 2015.
- [7] S. Rangan, P. Schniter, and A. K. Fletcher, “Vector approximate message passing,” *IEEE Trans. Inf. Theory*, vol. 65, no. 10, pp. 6664–6684, 2019.
- [8] J. Ma and L. Ping, “Orthogonal AMP,” *IEEE Access*, vol. 5, pp. 2020–2033, 2017.
- [9] S. Rangan, “Generalized approximate message passing for estimation with random linear mixing,” in *Proc. IEEE Int. Symp. Inf. Theory*, 2011, pp. 2168–2172.
- [10] Z. Xue, J. Ma, and X. Yuan, “Denoising-based turbo compressed sensing,” *IEEE Access*, vol. 5, pp. 7193–7204, 2017.
- [11] C. A. Metzler, A. Maleki, and R. G. Baraniuk, “BM3D-PRGAMP: Compressive phase retrieval based on BM3D denoising,” in *Proc. IEEE Int. Conf. Image Process.*, 2016, pp. 2504–2508.
- [12] T. Blu and F. Luisier, “The SURE-LET approach to image denoising,” *IEEE Trans. Image Process.*, vol. 16, no. 11, pp. 2778–2786, 2007.
- [13] K. Dabov, A. Foi, V. Katkovnik, and K. Egiazarian, “Image denoising with block-matching and 3D filtering,” in *Proc. SPIE Image Process.: Algorithms Syst., Neural Netw., Mach. Learn.*, vol. 6064, 2006, pp. 354–365.

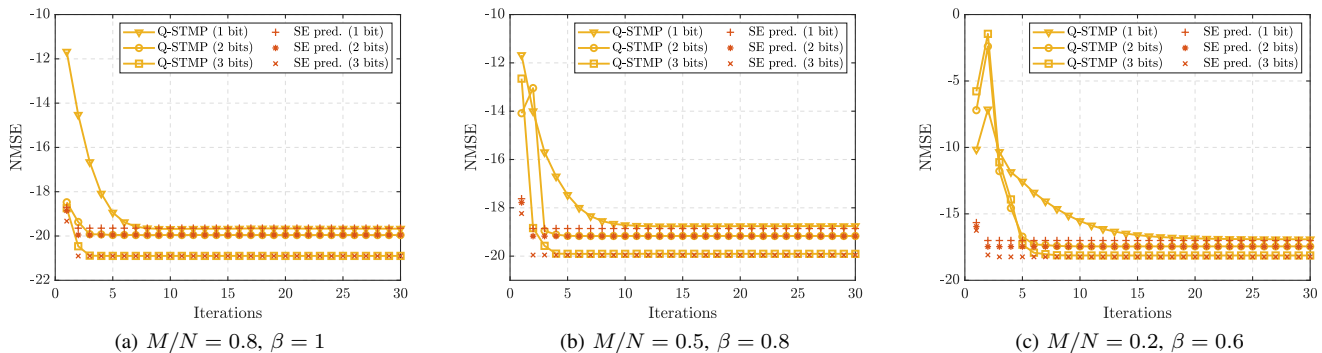


Fig. 8. Convergence behaviors and SE predictions of Q-STMP for different sampling ratios and quantization bit depths, where $\delta_0 = 0.5$.

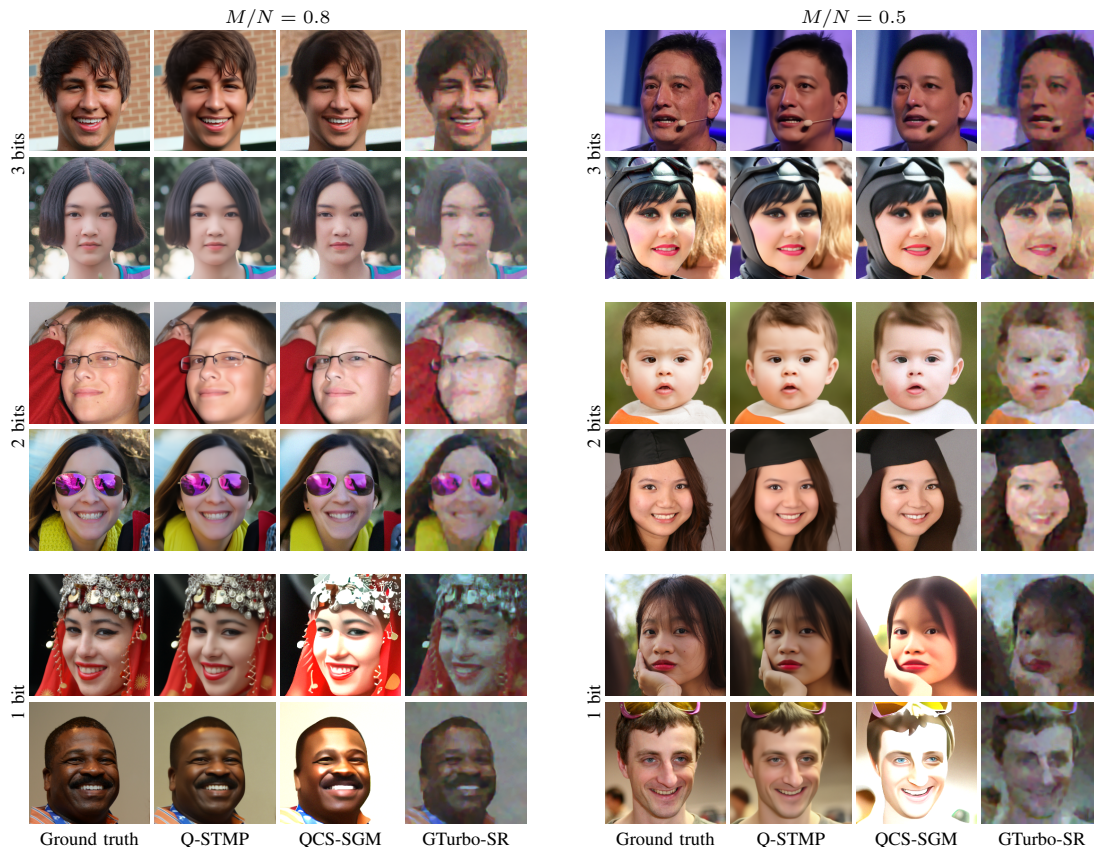


Fig. 9. Representative results for quantized compressive image recovery on the FFHQ validation set, where $\delta_0 = 0.1$. We set $\beta = 0.6$ for Q-STMP.

- [14] C. Metzler, A. Mousavi, and R. Baraniuk, “Learned D-AMP: Principled neural network based compressive image recovery,” in *Proc. Adv. Neural Inf. Process. Syst.*, vol. 30, 2017.
- [15] Z. Zhang, Y. Liu, J. Liu, F. Wen, and C. Zhu, “AMP-Net: Denoising-based deep unfolding for compressive image sensing,” *IEEE Trans. Image Process.*, vol. 30, pp. 1487–1500, 2021.
- [16] Y. Song and S. Ermon, “Generative modeling by estimating gradients of the data distribution,” in *Proc. Adv. Neural Inf. Process. Syst.*, vol. 32, 2019.
- [17] Y. Song, J. Sohl-Dickstein, D. P. Kingma, A. Kumar, S. Ermon, and B. Poole, “Score-based generative modeling through stochastic differential equations,” in *Proc. Int. Conf. Learn. Repr.*, 2021.
- [18] J. Ho, A. Jain, and P. Abbeel, “Denoising diffusion probabilistic models,” in *Proc. Adv. Neural Inf. Process. Syst.*, vol. 33, 2020, pp. 6840–6851.
- [19] A. Jalal, M. Arvinte, G. Daras, E. Price, A. G. Dimakis, and J. I. Tamir, “Robust compressed sensing MRI with deep generative priors,” in *Proc. Adv. Neural Inf. Process. Syst.*, 2021, pp. 14 938–14 954.
- [20] J. Choi, S. Kim, Y. Jeong, Y. Gwon, and S. Yoon, “ILVR: conditioning method for denoising diffusion probabilistic models,” in *Proc. IEEE Int. Conf. Comput. Vis.* IEEE, 2021, pp. 14 347–14 356.
- [21] X. Meng and Y. Kabashima, “Diffusion model based posterior sampling for noisy linear inverse problems,” in *Proc. Asian Conf. Mach. Learn.*, vol. 260. PMLR, 2024, pp. 623–638.
- [22] B. Kawar, M. Elad, S. Ermon, and J. Song, “Denoising diffusion restoration models,” in *Proc. Adv. Neural Inf. Process. Syst.*, vol. 35, 2022, pp. 23 593–23 606.
- [23] H. Chung, B. Sim, D. Ryu, and J. C. Ye, “Improving diffusion models for inverse problems using manifold constraints,” in *Proc. Adv. Neural Inf. Process. Syst.*, 2022.
- [24] H. Chung, J. Kim, M. T. McCann, M. L. Klasky, and J. C. Ye, “Diffusion posterior sampling for general noisy inverse problems,” in *Proc. Int. Conf. Learn. Repr.*, 2023.
- [25] J. Song, A. Vahdat, M. Mardani, and J. Kautz, “Pseudoinverse-guided diffusion models for inverse problems,” in *Proc. Int. Conf. Learn. Repr.*, 2023.
- [26] Y. Zhu, K. Zhang, J. Liang, J. Cao, B. Wen, R. Timofte, and L. V. Gool, “Denoising diffusion models for plug-and-play image restoration,” in *Proc. IEEE/CVF Conf. Comput. Vis. Pattern Recognit. Workshops.* IEEE, 2023, pp. 1219–1229.
- [27] B. Efron, “Tweedie’s formula and selection bias,” *J. Amer. Stat. Assoc.*, vol. 106, no. 496, pp. 1602–1614, 2011.
- [28] C. Meng, Y. Song, W. Li, and S. Ermon, “Estimating high order gradients of the data distribution by denoising,” in *Proc. Adv. Neural Inf. Process. Syst.*, vol. 34, 2021, pp. 25 359–25 369.

TABLE II
 QUANTITATIVE RESULTS FOR QUANTIZED COMPRESSIVE IMAGE RECOVERY ON THE FFHQ VALIDATION SET
 (BOLD: BEST, UNDERLINE: SECOND BEST; $\delta_0 = 0.1$)

Quantization	Method	$M/N = 0.8$				$M/N = 0.5$			
		PSNR \uparrow	SSIM \uparrow	FID \downarrow	LPIPS \downarrow	PSNR \uparrow	SSIM \uparrow	FID \downarrow	LPIPS \downarrow
3 bits	Q-STMP (Ours)	29.88	0.8660	44.98	0.1149	28.93	0.8453	48.74	0.1353
	QCS-SGM	26.88	0.7497	48.33	0.1514	26.02	0.7206	56.55	0.1879
	GTurbo-SR	22.81	0.6969	64.55	0.3158	22.98	0.6811	88.68	0.3998
2 bits	Q-STMP (Ours)	28.52	0.8364	48.78	0.1421	27.13	0.7919	48.65	0.1674
	QCS-SGM	24.86	0.7121	56.84	0.1943	23.95	0.6791	65.90	0.2351
	GTurbo-SR	20.70	0.6332	116.84	0.4669	20.14	0.5884	164.07	0.5530
1 bit	Q-STMP (Ours)	27.39	0.8268	48.04	0.1482	25.79	0.7411	47.10	0.1957
	QCS-SGM	12.17	0.5685	99.61	0.3573	11.34	0.5230	117.85	0.4109
	GTurbo-SR	18.72	0.6061	133.15	0.4946	18.10	0.5610	185.61	0.5626

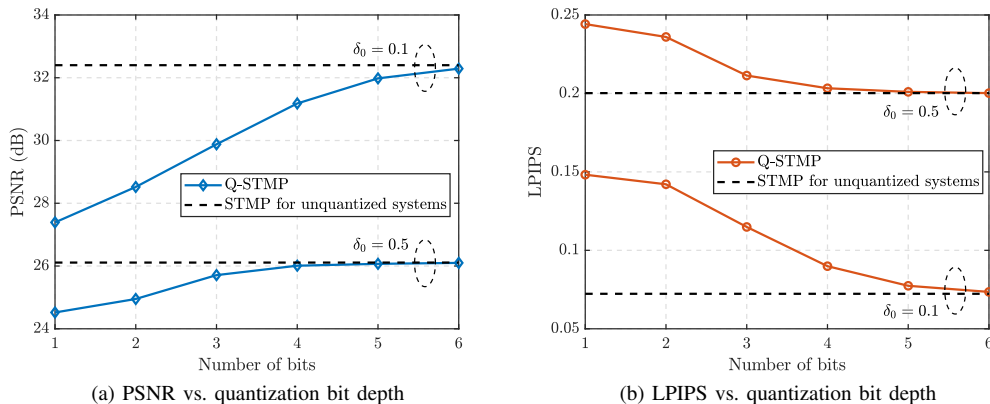


Fig. 10. Performance of Q-STMP under different quantization bit depths for a sampling ratio of $M/N = 0.8$. Dashed lines indicate the performance of STMP in the unquantized setting.

- [29] C. Lu, K. Zheng, F. Bao, J. Chen, C. Li, and J. Zhu, “Maximum likelihood training for score-based diffusion ODEs by high order denoising score matching,” in *Proc. Int. Conf. Mach. Learn.* PMLR, 2022, pp. 14 429–14 460.
- [30] T. P. Minka, “Expectation propagation for approximate Bayesian inference,” in *Proc. Conf. Uncertainty Artif. Intell.* Morgan Kaufmann, 2001, pp. 362–369.
- [31] X. Meng, S. Wu, and J. Zhu, “A unified Bayesian inference framework for generalized linear models,” *IEEE Signal Process. Lett.*, vol. 25, no. 3, pp. 398–402, 2018.
- [32] T. Karras, S. Laine, and T. Aila, “A style-based generator architecture for generative adversarial networks,” in *Proc. IEEE Conf. Comput. Vis. Pattern Recognit.* IEEE, 2019, pp. 4401–4410.
- [33] S. V. Venkatakrisnan, C. A. Bouman, and B. Wohlberg, “Plug-and-play priors for model based reconstruction,” in *Proc. IEEE Global Conf. Signal Inf. Process.*, 2013, pp. 945–948.
- [34] S. H. Chan, X. Wang, and O. A. Elgindy, “Plug-and-play ADMM for image restoration: Fixed-point convergence and applications,” *IEEE Trans. Comput. Imaging*, vol. 3, no. 1, pp. 84–98, 2017.
- [35] X. Wang and S. H. Chan, “Parameter-free plug-and-play ADMM for image restoration,” in *Proc. IEEE Int. Conf. Acoust., Speech, Signal Process.*, 2017, pp. 1323–1327.
- [36] Y. Sun, B. Wohlberg, and U. S. Kamilov, “An online plug-and-play algorithm for regularized image reconstruction,” *IEEE Trans. Comput. Imaging*, vol. 5, no. 3, pp. 395–408, 2019.
- [37] K. Zhang, W. Zuo, S. Gu, and L. Zhang, “Learning deep CNN denoiser prior for image restoration,” in *Proc. IEEE Conf. Comput. Vis. Pattern Recognit.*, 2017, pp. 3929–3938.
- [38] K. Zhang, Y. Li, W. Zuo, L. Zhang, L. Van Gool, and R. Timofte, “Plug-and-play image restoration with deep denoiser prior,” *IEEE Trans. Pattern Anal. Mach. Intell.*, vol. 44, no. 10, pp. 6360–6376, 2022.
- [39] Y. Romano, M. Elad, and P. Milanfar, “The little engine that could: Regularization by denoising (RED),” *SIAM J. Imag. Sci.*, vol. 10, no. 4, pp. 1804–1844, 2017.
- [40] R. Cohen, M. Elad, and P. Milanfar, “Regularization by denoising via fixed-point projection (RED-PRO),” *SIAM J. Imag. Sci.*, vol. 14, no. 3, pp. 1374–1406, 2021.
- [41] E. T. Reehorst and P. Schniter, “Regularization by denoising: Clarifications and new interpretations,” *IEEE Trans. Comput. Imaging*, vol. 5, no. 1, pp. 52–67, 2019.
- [42] Z. Xue, P. Cai, X. Yuan, and X. Gao, “Score-based reverse mean propagation for solving inverse problems,” *IEEE Trans. Signal Process.*, vol. 73, pp. 3947–3962, 2025.
- [43] J. Song, C. Meng, and S. Ermon, “Denoising diffusion implicit models,” in *Proc. Int. Conf. Learn. Repr.*, 2021.
- [44] M. Mardani, J. Song, J. Kautz, and A. Vahdat, “A variational perspective on solving inverse problems with diffusion models,” in *Proc. Int. Conf. Learn. Repr.*, 2024.
- [45] H.-J. M. Shi, M. Case, X. Gu, S. Tu, and D. Needell, “Methods for quantized compressed sensing,” in *Proc. IEEE Inf. Theory Appl. Workshop*, 2016, pp. 1–9.
- [46] U. S. Kamilov, V. K. Goyal, and S. Rangan, “Message-passing dequantization with applications to compressed sensing,” *IEEE Trans. Signal Process.*, vol. 60, no. 12, pp. 6270–6281, 2012.
- [47] T. Liu, C.-K. Wen, S. Jin, and X. You, “Generalized turbo signal recovery for nonlinear measurements and orthogonal sensing matrices,” in *Proc. IEEE Int. Symp. Inf. Theory*, 2016, pp. 2883–2887.
- [48] X. Meng and Y. Kabashima, “Quantized compressed sensing with score-based generative models,” in *Proc. Int. Conf. Learn. Repr.*, 2023.
- [49] —, “QCS-SGM+: Improved quantized compressed sensing with score-based generative models,” in *Proc. AAAI Conf. Artif. Intell.*, vol. 38, no. 13, 2024, pp. 14 341–14 349.
- [50] A. K. Fletcher, P. Pandit, S. Rangan, S. Sarkar, and P. Schniter, “Plug-in estimation in high-dimensional linear inverse problems: A rigorous analysis,” in *Proc. Adv. Neural Inf. Process. Syst.*, 2018, pp. 7451–7460.
- [51] C. Berrou and A. Glavieux, “Near optimum error correcting coding and decoding: Turbo-codes,” *IEEE Trans. Commun.*, vol. 44, no. 10, pp. 1261–1271, 1996.
- [52] H. E. Robbins, “An empirical Bayes approach to statistics,” in *Breakthroughs in Stat.: Found. and Basic Theory*. Springer, 1992, pp. 388–394.
- [53] P. Vincent, “A connection between score matching and denoising autoencoders,” *Neural Comput.*, vol. 23, no. 7, pp. 1661–1674, 2011.